Check for updates

Chemistry – A European Journal

ChemEurJ Chemistry Europe European Chemical Societies Publishing

RESEARCH ARTICLE OPEN ACCESS

Synthesis and Optical Properties of Diboron Complexes of 1,4-Anthraquinone Derivatives

Yasuhiro Kubota[1] | Ayumi Ogasawara[1] | Ayato Hakamada[2] | Naoya Suzuki[3] | Masayasu Taki[3] | Shota Mizuno[1] | Toshiyasu Inuzuka[4] | Kazumasa Funabiki[1] | Chie Yamada-Kubota[5] | Miho Kuwahara[5] | Tetsuya Hara[5]

[1]Department of Chemistry and Biomolecular Science, Faculty of Engineering, Gifu University, Gifu, Japan | [2]Department of Chemistry, Graduate School of Science, Nagoya University, Nagoya, Japan | [3]Institute For Glyco-core Research (iGCORE), Gifu University, Gifu, Japan | [4]Life Science Research Center, Gifu University, Gifu, Japan | [5]Department of Occlusal and Oral Functional Rehabilitation, Graduate School of Medicine, Dentistry, and Pharmaceutical Sciences, Okayama University, Okayama, Japan

Correspondence: Yasuhiro Kubota (kubota.yasuhiro.u8@f.gifu-u.ac.jp)

Received: 26 February 2026 | **Revised:** 2 May 2026 | **Accepted:** 14 May 2026

Keywords: anthraquinone | boron complex | near infrared fluorescence | photoinduced electron transfer | β-Iminoenolate structure

ABSTRACT

NˆO-type 1,4-diboron complexes (**5**: R = H, **6**: R = CF_3, **7**: R = OMe, and **8**: R = NMe_2) were synthesized via a simple two-step reaction and their photophysical properties were systematically investigated. Single-crystal x-ray diffraction analysis of **5** revealed a planar diboron chromophore with two β-iminoenolate structures, while the *N*-phenyl substituents are significantly twisted from the chromophore plane. Boron complexation rigidified the chromophore, affording vibronically resolved and spectrally narrowed absorption bands for **5**–**7**, whereas **8** exhibited pronounced spectral broadening accompanied by a bathochromic shift. TDDFT calculations indicated that increasing electron-donating ability shifts the S_0–S_2 transition to longer wavelengths, and in **8** this transition overlaps with S_0–S_1, accounting for the spectral broadening. Complexes **5**–**7** exhibited near-infrared fluorescence, while **8** was nonfluorescent. Dynamic quenching of **5** by *N*,*N*-dimethylaniline via intermolecular photoinduced electron transfer (PeT) was confirmed by Stern–Volmer analysis with lifetime shortening. The decrease in fluorescence quantum yield with increasing electron-donating ability was attributed to intramolecular PeT, and protonation restored fluorescence. The nonfluorescent nature of the 1,5-diboron complex was attributed to enhanced nonradiative decay in accordance with the energy gap law, together with possible intramolecular PeT.

1 | Introduction

Organoboron complexes represent a prominent class of fluorescent dyes [1–6]. Among them, BODIPY (4,4-difluoro-4-bora-3a,4a-diaza-*s*-indacene) dye is the most well-known and has been the subject of numerous comprehensive reviews [7–12]. BODIPY dyes comprise dipyrromethene cores rigidified via a nitrogen–boron–nitrogen (N–B–N) bridging motif. This structural rigidification suppresses non-radiative decay pathways, thereby enhancing the fluorescence quantum yield (Φ_f) of the ligand dye. Moreover, the photophysical properties of organoboron complexes are highly dependent on the structure of the dye ligand. Therefore, boron complexation of organic dyes offers an effective strategy for the development of novel fluorescent materials. Indeed, organoboron complexes have been extensively explored for applications across diverse fields, including optoelectronics [13–16] and biomedicine [17–20]. The design and synthesis of new boron-based complexes remain an area of active research [21–28].

On the other hand, natural anthraquinones were historically employed as the principal dyes in textile applications [29, 30].

This is an open access article under the terms of the Creative Commons Attribution License, which permits use, distribution and reproduction in any medium, provided the original work is properly cited.
© 2026 The Author(s). *Chemistry – A European Journal* published by Wiley-VCH GmbH.

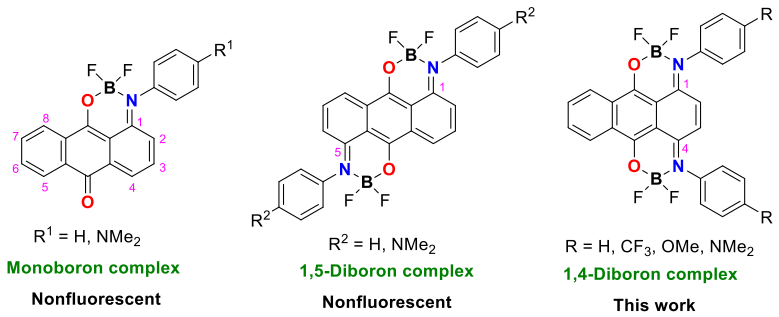

FIGURE 1 | N^O-type boron complexes of anthraquinone.

Even today, anthraquinone derivatives remain widely applied in various colorant applications, including textiles and food products [31, 32]. In addition, anthraquinones are well known for their remarkable anticancer properties, leading to the design and synthesis of numerous novel derivatives with a wide range of biological activities [33]. Anthraquinone derivatives are widely employed in various applications such as colorimetric sensors [34, 35], non-linear optical (NLO) materials [36], liquid crystals [37, 38] and hydrogen peroxide production [39, 40], owing to their exceptional thermal and photochemical stability, coordination ability, electron-accepting properties, rigid molecular framework, and reversible redox behavior. Some substituted anthraquinones exhibit fluorescence. Anthraquinones possessing a low-energy π,π^* state are particularly prone to fluorescence [41]. Anthraquinones displaying solvatochromic fluorescence [42, 43], aggregation-induced emission (AIE) [44, 45], mechanochromic luminescence (MCL) [46, 47], and thermally activated delayed fluorescence (TADF) [48, 49] have been reported. Owing to these fluorescence properties, anthraquinones have been applied in image-guided photodynamic therapy [50], intracellular reactions [51], fluorescent imaging [52], and organic light-emitting diodes (OLEDs) [53]. There have been only a few reports on boron complexes of anthraquinone. Although the synthesis of O^O-type boron complexes of anthraquinone has been reported by P. N. Preston et al. [54, 55] and H. Hartmann et al. [56], and that of N^O-type boron complexes by M. V. Gorelik et al. [57], their optical properties are not reported in the literature. For O^O-type boron complexes of anthraquinone, K. Ono et al. reported that naphthacenequinone-based complexes exhibit fluorescence [58, 59]. In the context of N^O-type boron complexes of anthraquinone, we previously reported that monoboron and 1,5-diboron complexes exhibit near-infrared panchromatic absorption without detectable fluorescence (Figure 1) [60]. In this study, we report the synthesis and photophysical properties of 1,4-diboron complexes derived from 1,4-bis(arylamino)anthraquinone (Figures 1, R = H, CF_3, OMe, NMe_2), demonstrating that, in contrast to the 1,5-analogues, these complexes exhibit near-infrared fluorescence. The fluorescence quantum yields were found to decrease with increasing electron-donating ability of the substituent R. Mechanistic investigations revealed that this quenching predominantly arises from intramolecular photoinduced electron transfer (PeT), as supported by intermolecular PeT quenching experiments upon addition of dimethylaminobenzene (DMA) to 1,4-diboron complex **5** (R = H). Furthermore, DFT calculations suggest that intramolecular PeT is more favorable in 1,5-diboron complexes than in the 1,4 counterparts, thereby providing new insight into the structure–property relationship governing emissive versus non-emissive behavior in diboron complexes of anthraquinone.

2 | Synthesis

1,4-Bis(arylamino)anthraquinones **1** [61], **3** [62], and **4** [63] are known compounds. Compounds **1**–**4** were synthesized by the reaction of 1,4-dihydroxyanthraquinone with various aniline derivatives, as shown in Scheme 1. In this reaction, 1,4-dihydroxyanthraquinone was first reduced with hydrogen to yield leucoquinizarin, which subsequently reacted with aniline derivatives in the presence of boric acid to afford the corresponding 1,4-bis(arylamino)anthraquinones. The resulting anthraquinones **1**–**4** were then treated with boron trifluoride–diethyl ether complex to yield the corresponding boron complexes **5**–**8** (Scheme 1). In the ^{13}C NMR spectra of compounds **1**–**4** and **6**–**8** recorded in $CDCl_3$, the two aryl groups on the nitrogen atoms exhibited non-equivalent carbon signals, indicating restricted rotation or asymmetry around the nitrogen centers.

3 | Crystal Structures

Single crystal of **5** was obtained by slow diffusion of *n*-hexane into a solution of **5** in dichloromethane. The x-ray crystallographic structures of **5** is shown in Figure 2. The chromophore of **5**, namely, the anthraquinone–diboron moiety, is highly planar and adopts an asymmetric structure in the crystalline state. The dihedral angles between the anthraquinone–diboron moiety and the two phenyl groups are 84.2° and 66.1°, respectively. Experimentally obtained bond lengths of **5** in the crystalline state are shown in Figure S1. The C1—C11 and C4—C12 bond lengths (both 1.43 Å) are longer than those of C9—C11 (1.38 Å) and C10—C12 (1.39 Å). The C1—N1 (1.32 Å) and C4—N2 (1.33 Å) bond lengths are more similar to that of a typical C=N double bond (ca. 1.29 Å) than to that of a C—N single bond (ca. 1.47 Å) [64]. Additionally, the C9—O1 and C10—O2 bond lengths (both 1.32 Å) are intermediate between those of a typical single C—O bond (ca. 1.42 Å) and a typical double C=O bond (ca. 1.22 Å) [64]. These results suggest that the bidentate ligand of **5** adopts a delocalized β-iminoenolate structure rather than the β-ketoiminate structure in the crystalline state (Figure S2).

15213765, 2026, 34, Downloaded from https://chemistry-europe.onlinelibrary.wiley.com/doi/10.1002/chem.71179 by Okayama University, Wiley Online Library on [19/11/2026]. See the Terms and Conditions (https://onlinelibrary.wiley.com/terms-and-conditions) on Wiley Online Library for rules of use; OA articles are governed by the applicable Creative Commons License

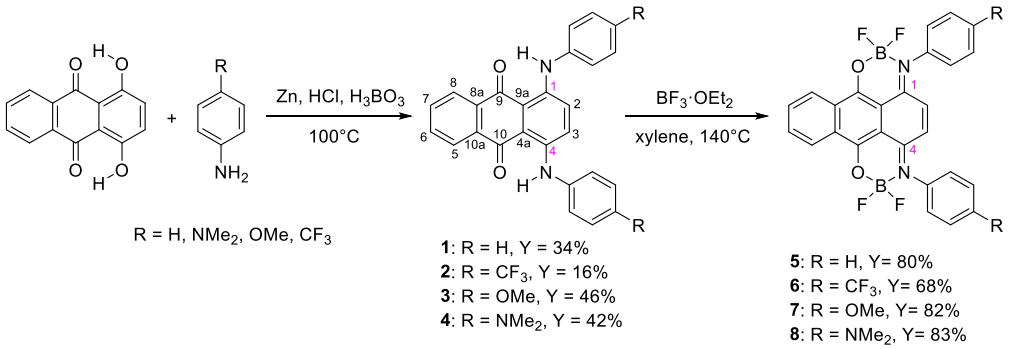

SCHEME 1 | Synthesis of diboron complexes **5**–**8** derived from 1,4 bis(arylamino)anthraquinone.

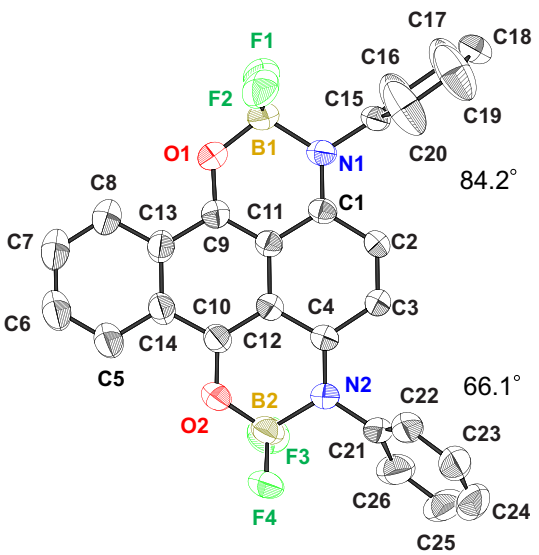

FIGURE 2 | ORTEP drawing of **5**. Hydrogen atoms are omitted for clarity. The dihedral angles between the anthraquinone moiety and the phenyl ring are shown.

TABLE 1 | UV-vis-NIR absorption properties in dichloromethane.

Compd	λ_{max}/nm (ε)	fwhm[a] (cm^{-1})
1	400 (7,700), 598 (16,400), 640 (17,300)	3,140
2	396 (13,000), 587 (16,100), 625 (15,700)	3,310
3	410(5,900), 639 (16,000)	3,170
4	477 (5,100), 651 (16,500)	3,440
5	414 (8,300), 496 (3,100), 532 (9,200), 576 (20,800), 628 (25,400)	2,280
6	412 (9,000), 496 (3,200), 532 (10,300), 576 (24,700), 628 (32,500)	2,180
7	493 (8,400), 540 (9,800), 585 (18,400), 637 (20,700)	2,660
8	680 (21,900)	4,900

[a]Full width at half-maximum height.

4 | UV–Vis–NIR Absorption Properties

The UV–Vis–NIR absorption spectra of 1,4-bis(arylamino)anthraquinones **1**–**4** and 1,4-diboron complexes **5**–**8** in dichloromethane are shown in Figure 3. The maximum absorption wavelengths (λ_{max}), molar extinction coefficients (ε), and full widths at half-maximum (fwhm) are summarized in Table 1. Boron complexation rigidifies the chromophore, leading to distinct vibrational peaks in the absorption spectra of complexes **5**–**7**. For example, in the spectrum of **5**, the peaks at 628, 576, 532, and 496 nm are assigned to the $S_{0,0}$–$S_{1,0}$, $S_{0,0}$–$S_{1,1}$, $S_{0,0}$–$S_{1,2}$, and $S_{0,0}$–$S_{1,3}$ transitions, respectively.

To obtain a deeper insight into the absorption properties, density functional theory (DFT) calculations were performed [65]. Geometry optimization was performed at the B3LYP/6-31G(d,p) level. Electronic transitions were also calculated using the time dependent DFT (TDDFT) method [66–68] at the B3LYP/6-31G(d,p) level. The molecular orbital energy diagrams and isodensity surface plots of **1**–**8** are shown in Figure 4. The calculated λ_{max} values, principal orbital transitions and oscillator strength (f) values of **1**–**8** are presented in Table 2. TDDFT calculations revealed that the S_0–S_1 transitions of compounds **1**–**8** are primarily attributed to HOMO–LUMO excitations. The LUMO orbitals of all compounds exhibit similar characteristics, being predominantly delocalized over the anthraquinone moiety. In contrast, the HOMO orbitals display significant differences between the 1,4-bis(arylamino)anthraquinones **1**–**4** and their corresponding boron complexes **5**–**8**. For compounds **1**–**4**, the HOMO orbitals are delocalized over the aryl groups attached to the nitrogen atoms and only partially over the anthraquinone core. In contrast, the HOMO orbitals of the boron complexes **5**–**8** are delocalized over both the aryl groups on the nitrogen atoms and nearly the entire anthraquinone moiety. Consequently, unlike **5**–**8**, the HOMO orbitals of **1**–**4** exhibit negligible delocalization over the A moiety, as exemplified by compound **1** in Figure 4.

The previously reported unsubstituted 1,5-anthraquinone (λ_{max} = 530 nm, fwhm = 3,880 cm^{-1}) exhibited a pronounced bathochromic shift of 164 nm in λ_{max} and a narrowing of the spectral features upon boron complexation (diboron complex: λ_{max} = 694 nm, fwhm = 2,510 cm^{-1}) (Figure S3) [60]. In contrast, the corresponding unsubstituted 1,4-anthraquinone **1** (λ_{max} = 640 nm, fwhm = 3,140 cm^{-1}) also showed spectral narrowing upon boron complexation, but the λ_{max} underwent

15213765, 2026, 34, Downloaded from https://chemistry-europe.onlinelibrary.wiley.com/doi/10.1002/chem.71179 by Okayama University, Wiley Online Library on [19/11/2026]. See the Terms and Conditions (https://onlinelibrary.wiley.com/terms-and-conditions) on Wiley Online Library for rules of use; OA articles are governed by the applicable Creative Commons License

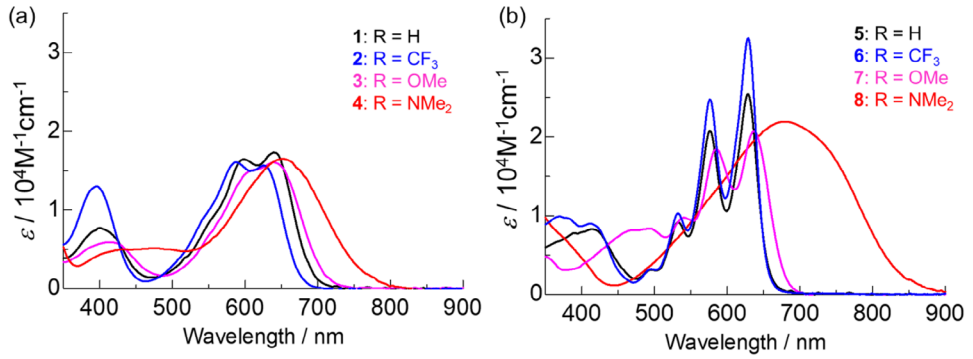

FIGURE 3 | UV–vis–NIR absorption spectra of (a) 1,4-bis(arylamino)anthraquinones **1**–**4** and (b) 1,4-diboron complexes **5**–**8** in dichloromethane.

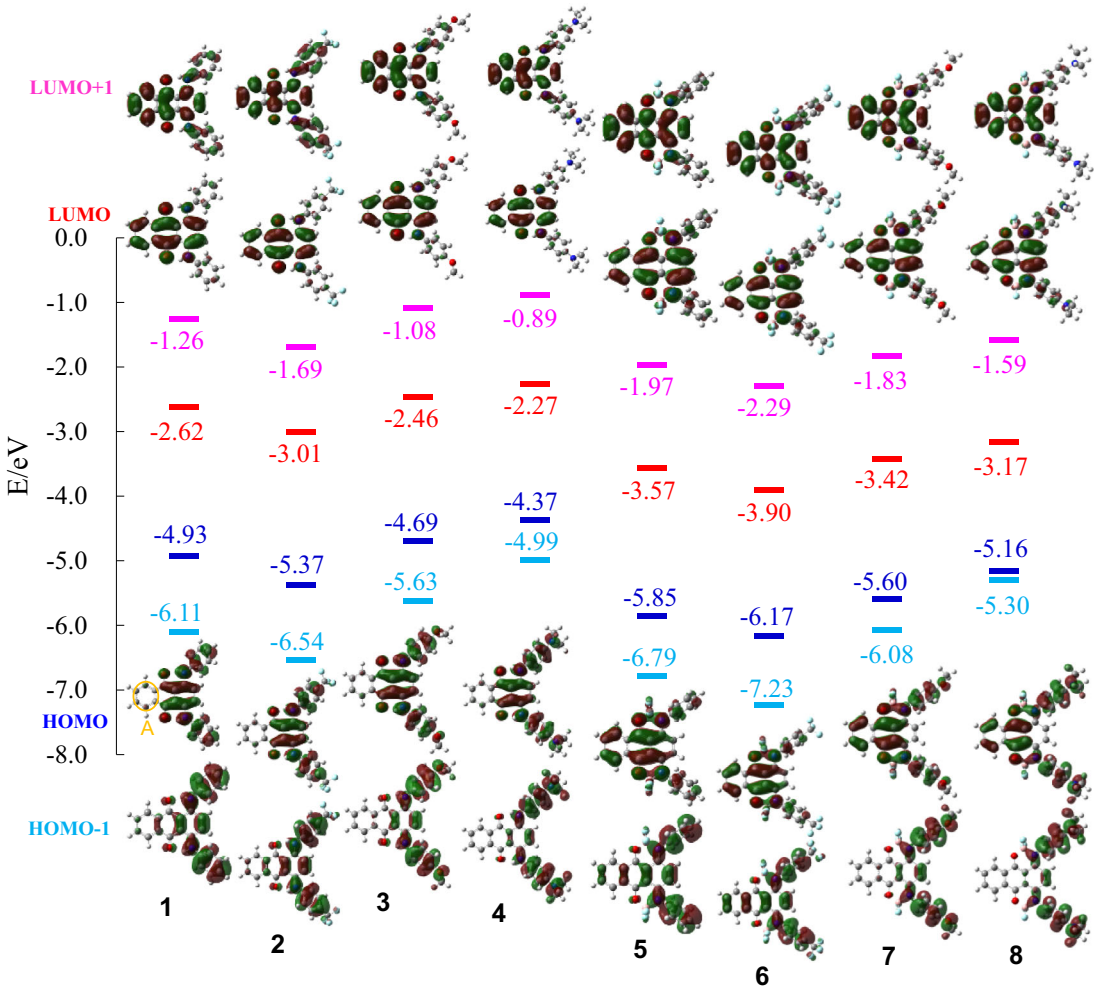

FIGURE 4 | Molecular orbital energy diagrams and isodensity surface plots of **1**–**8**.

a hypsochromic shift (**5**: λ_{max} = 628 nm, fwhm = 2,280 cm^{-1}) (Table 1). The observed spectral narrowing upon boron complexation is attributed to the rigidification of the anthraquinone skeleton. Both the S_0–S_1 (HOMO–LUMO) transitions of **1** and **5** correspond to intramolecular charge-transfer (ICT) transitions from the two terminal aminophenyl groups to the anthraquinone moiety. The absence of a pronounced bathochromic shift upon boron complexation of **1** is attributed to the differences between the HOMOs of **1** and **5**. The lack of delocalization in the A portion of **1** suggests that its HOMO is more localized (Figure 4), resulting in a greater contribution of the ICT transition in **1** than in **5**. As a result, although boron complexation increases the electron-withdrawing character of the anthraquinone moiety, the ICT contribution is reduced, leading to a slight hypsochromic shift of λ_{max}.

Similarly, the trifluoromethyl derivative **2** (λ_{max} = 625 nm, fwhm = 3,310 cm^{-1}) and the methoxy derivative **3** (λ_{max} = 639 nm, fwhm

15213765, 2026, 34, Downloaded from https://chemistry-europe.onlinelibrary.wiley.com/doi/10.1002/chem.71179 by Okayama University, Wiley Online Library on [19/11/2026]. See the Terms and Conditions (https://onlinelibrary.wiley.com/terms-and-conditions) on Wiley Online Library for rules of use; OA articles are governed by the applicable Creative Commons License

TABLE 2 | Absorption maxima (λ_{max}), oscillator strengths (f), and main orbital transition calculated by TDDFT at the B3LYP/6-31G(d,p) level.

Compd	Transition	λ_{max} (nm)	Main orbital transition	f
1	S_0 to S_1	596	HOMO to LUMO (0.71)	0.23
	S_0 to S_2	424	HOMO-1 to LUMO (0.68)	0.08
2	S_0 to S_1	588	HOMO to LUMO (0.71)	0.23
	S_0 to S_2	419	HOMO-1 to LUMO (0.68)	0.07
3	S_0 to S_1	615	HOMO to LUMO (0.71)	0.24
	S_0 to S_2	464	HOMO-1 to LUMO (0.70)	0.11
4	S_0 to S_1	655	HOMO to LUMO (0.71)	0.24
	S_0 to S_2	541	HOMO-1 to LUMO (0.70)	0.13
5	S_0 to S_1	595	HOMO to LUMO (0.71)	0.26
	S_0 to S_2	448	HOMO-1 to LUMO (0.70)	0.23
6	S_0 to S_1	594	HOMO to LUMO (0.71)	0.27
	S_0 to S_2	432	HOMO-1 to LUMO (0.69)	0.25
7	S_0 to S_1	632	HOMO to LUMO (0.71)	0.27
	S_0 to S_2	550	HOMO-1 to LUMO (0.70)	0.26
8	S_0 to S_1	704	HOMO to LUMO (0.71)	0.28
	S_0 to S_2	682	HOMO-1 to LUMO (0.71)	0.32

= 3,170 cm^{-1}) exhibited spectral narrowing upon boron complexation, while their λ_{max} values remained nearly unchanged (**6**: λ_{max} = 628 nm, fwhm = 2,180 cm^{-1}, **7**: λ_{max} = 637 nm, fwhm = 2,660 cm^{-1}). On the other hand, the boron complexation of the dimethylamino derivative **4** (λ_{max} = 651 nm, fwhm = 3,440 cm^{-1}) induced a bathochromic shift of λ_{max} along with spectral broadening (**8**: λ_{max} = 680 nm, fwhm = 4,900 cm^{-1}). According to TDDFT calculations, the S_0–S_1 and S_0–S_2 transitions of **8** are located at similar wavelengths, and their overlap is considered to contribute to the observed spectral broadening (Table 2). The S_0–S_2 transitions of **5**, **6**, and **7** were observed at 414, 412, and 493 nm, respectively, whereas the S_0–S_2 transition of **8** was observed to overlap with the S_0–S_1 transition (Table 1). This suggests that the S_0–S_2 transition shifts to longer wavelengths as the electron-donating ability of the substituent R increases. The S_0–S_2 transition of **5**–**8** was assigned to the HOMO–1 to LUMO excitation. Focusing on the HOMO−1 orbitals of **5**–**8**, the electron density in **5** and **6** is delocalized over the two aryl groups and the anthraquinone moiety, whereas in **7** and **8** bearing electron-donating substituents, it is predominantly localized on the two aryl groups. In particular, this localization is most pronounced for **8** containing two dimethylamino groups. In contrast, no significant differences are observed in the LUMO orbitals of **5**–**8**. These calculation results suggest that, as the electron-donating ability of substituent R increases, the contribution of ICT character to the S_0–S_2 (HOMO–1 to LUMO) transition becomes larger, leading to a red shift of the S_0–S_2 transition.

The cyclic voltammograms of **5**–**8** were measured in acetonitrile (Figure S4). For **5**, the first reduction half-wave potential ($E_{1/2}$ (red)) was −0.61 V (vs. Fc/Fc^+). In acetonitrile, the conversion of $E_{1/2}$ (vs. Fc/Fc^+) to $E_{1/2}$ (vs. NHE) is known to be as follows: $E_{1/2}$ (vs. NHE) = $E_{1/2}$ (vs. Fc/Fc^+) + 0.63 V [69]. Therefore, the first $E_{1/2}$ (red) value related to the LUMO energy level (E_{LUMO}) of **5** was estimated to be 0.02 V (vs. NHE) (Table S1). The HOMO energy level (E_{HOMO}) of **5** was estimated to be 1.87 V (vs. NHE) by adding the zero–zero excitation energy ($E_{0\text{-}0}$), estimated from the absorption onset wavelength in dichloromethane (670 nm, 1.85 eV), to the corresponding E_{LUMO} value (Table S1). Similarly, the E_{HOMO} and E_{LUMO} values for compounds **6**–**8** were estimated (Table S1). These values showed good correlation with those obtained from DFT calculations (Figure 4).

5 | Fluorescence Properties

1,4-Bis(arylamino)anthraquinones **1**–**4** exhibited no fluorescence. In contrast, among the boron complexes, the non-, trifluoromethyl- and methoxy-substituted derivatives **5**, **6**, and **7** showed fluorescence, whereas the dimethylamino-substituted derivative **8** did not show fluorescence in dichloromethane (Figure 5). The maximum fluorescence wavelength (F_{max}) **5**, **6**, and **7** were observed at 652, 648, and 683 nm, respectively (Table 3). The fluorescence spectra of **5** and **6** were mirror images of the absorption spectra with very small Stokes shifts, indicating only minor geometrical differences between the ground and excited states [70] (Figure S5). The observed peaks are attributable to vibrational levels, as in the absorption spectra. For example, in the fluorescence spectrum of **5**, the peaks at 650, 707, and 767 nm are assigned to the $S_{1,0}$–$S_{0,0}$, $S_{1,0}$–$S_{0,1}$, and $S_{1,0}$–$S_{0,2}$ transitions, respectively. The fluorescence quantum yield (Φ_f) decreased as the electron-donating ability of substituent R increased (**5**: Φ_f = 0.15, **6**: Φ_f = 0.25, **7**: Φ_f = 0.02, **8**: Φ_f = 0.00). Time-resolved fluorescence decay measurements revealed fluorescence lifetimes (τ_s) of **5**, **6** and **7** of 3.48, 5.38 and 0.46 ns, respectively, with their decay profiles well-fitted by monoexponential functions. The radiative (k_f) and nonradiative (k_{nr}) rate constants were also calculated (Table 3). For compounds **5**–**7**, the k_f values were

15213765, 2026, 34, Downloaded from https://chemistry-europe.onlinelibrary.wiley.com/doi/10.1002/chem.71179 by Okayama University, Wiley Online Library on [19/11/2026]. See the Terms and Conditions (https://onlinelibrary.wiley.com/terms-and-conditions) on Wiley Online Library for rules of use; OA articles are governed by the applicable Creative Commons License

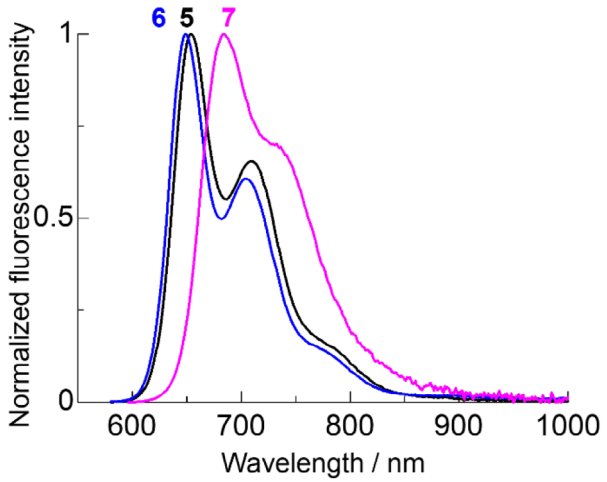

FIGURE 5 | Normalized fluorescence spectra of 1,4-diboron complexes in dichloromethane (3.0×10^{-5} M).

TABLE 3 | Fluorescence properties of 1,4-diboron complexes in dichloromethane[a].

Compd	F_{max} (nm)	Φ_f [b,c]	τ_s [d] (ns)	k_f [e] (10^9 s^{-1})	k_{nr} [f] (10^9 s^{-1})
5	652, 706, 777	0.15	3.48	0.043	0.24
6	648, 701, 771	0.25	5.38	0.046	0.14
7	683, 740	0.02	0.46	0.043	2.1
8	—[g]				

[a]Measured at a concentration of 3.0×10^{-5} M.
[b]The excitation wavelengths (λ_{ex}) were as follows: **5** (550 nm), **6** (550 nm) and **7** (550 nm).
[c]Measured using an integrating sphere method.
[d]Measured using a single-photon-counting method.
[e]Radiative rate constant ($k_f = \Phi_f/\tau_s$).
[f]Non-radiative rate constant ($k_{nr} = (1 - \Phi_f)/\tau_s$).
[g]Not observed.

nearly identical (**5**: k_f = 0.043×10^9 s^{-1}, **6**: k_f = 0.046×10^9 s^{-1}, **7**: k_f = 0.043×10^9 s^{-1}), whereas the k_{nr} values were observed to decrease markedly as the electron-donating ability of substituent R increased (**5**: k_{nr} = 0.24×10^9 s^{-1}, **6**: k_{nr} = 0.14×10^9 s^{-1}, **7**: k_{nr} = 2.1×10^9 s^{-1}). These results suggest that the decrease in the Φ_f value originates from the enhancement of nonradiative processes.

ICT-type dyes are generally known to exhibit decreased fluorescence intensity in polar solvents [71, 72]. To investigate the effect of solvent polarity, the fluorescence spectra of boron complexes **5**–**8** were measured in 1,4-dioxane (relative permittivity = 2.2), which is less polar than dichloromethane (relative permittivity = 8.9). As a result, the dimethylamino-substituted derivative **8** remained non-emissive in 1,4-dioxane, whereas **5**–**7** exhibited fluorescence (Figure S6). The F_{max} and Φ_f values were as follows (**5**: F_{max} = 654 nm, Φ_f = 0.16; **6**: F_{max} = 649 nm, Φ_f = 0.26; **7**: F_{max} = 684 nm, Φ_f = 0.03). Thus, trends similar to those observed in dichloromethane were observed. These results suggest that the non-emissive nature of **8** and the relatively low Φ_f of **7** cannot be sufficiently explained solely by solvent polarity.

Next, to examine the effect of substituent rotation and vibration on fluorescence quenching, the fluorescence spectra of **5** and **7** were measured in mixed solvents of methanol (0.55 cP) and ethylene glycol (23.5 cP) with varying viscosity. For **5**, no significant change in F_{max} (645 nm) was observed with increasing ethylene glycol content, whereas the fluorescence intensity decreased (Figure S7a). This result suggests that changes in the solvent environment (including increased dielectric constant and specific interactions), rather than suppression of intramolecular rotation and vibration due to increased viscosity, may contribute to the observed quenching. For **7**, increasing the proportion of ethylene glycol resulted in a slight red shift of F_{max} from 674 to 680 nm, accompanied by a substantial decrease in fluorescence intensity (Figure S7b). This behavior is consistent with a greater contribution of the ICT transition in **7** compared to **5**, leading to enhanced sensitivity to changes in the solvent environment. These results suggest that intramolecular rotation and vibration do not play a major role in the relatively low fluorescence quantum yield observed upon introduction of the methoxy group.

To examine the origin of the increase in the k_{nr} value with increasing electron-donating ability of the substituent R, dimethylaminobenzene (DMA), an electron donor, was added to **5** in dichloromethane. No significant change was observed in the absorption spectra (Figure 6a). In contrast, the fluorescence intensity decreased with increasing amounts of DMA (Figure 6b). To clarify the fluorescence quenching mechanism, Stern–Volmer analyses were performed (Figure 7a). The Stern–Volmer plot exhibited good linearity (R^2 = 0.997), indicating the presence of a single dominant quenching process. From the slope of the Stern–Volmer plot, a Stern–Volmer quenching constant K_{SV} of 72.3 M^{-1} was obtained. Because no ground-state interaction between DMA and **5** was detected in the absorption spectra (Figure 6a), static quenching is unlikely. Time-resolved fluorescence decay measurements were then carried out to probe the excited-state interaction (Figure 7b). The fluorescence lifetime of **5** was found to decrease progressively with increasing DMA concentration, demonstrating a dynamic quenching process. The measured τ_s values were 3.48, 3.19, 2.97, 2.46, 1.86, 1.49, and 1.27 ns at DMA concentrations of 0, 1.5, 3.0, 7.5, 15, 22.5, and 30 mM, respectively. On the basis of these results, the observed fluorescence quenching is attributed to dynamic intermolecular photoinduced electron transfer (PeT) from DMA to **5** [73–75]. This DMA quenching experiment serves as a model system for intermolecular electron transfer and supports the interpretation that the decrease in Φ_f observed for the 1,4-diboron complexes with increasing electron-donating ability of the substituent R originates from intramolecular PeT.

To obtain qualitative insight into the relative electron-donating abilities of the donor moieties, the HOMO energies of the isolated donor units were calculated at the B3LYP/6-31G(d,p) level. As shown in Figure S8, the calculated HOMO energies follow the order **8**> **7**> **5**> **6**, which correlates well with the experimentally observed fluorescence quenching efficiencies. These results support that the enhanced electron-donating ability of the donor moiety facilitates intramolecular PeT upon photoexcitation.

Trifluoroacetic acid (TFA) was added to the nonfluorescent dimethylamino derivative **8** to investigate protonation of the dimethylamino groups. The UV−vis−NIR absorption spectra of **8**

15213765, 2026, 34, Downloaded from https://chemistry-europe.onlinelibrary.wiley.com/doi/10.1002/chem.71179 by Okayama University, Wiley Online Library on [19/11/2026]. See the Terms and Conditions (https://onlinelibrary.wiley.com/terms-and-conditions) on Wiley Online Library for rules of use; OA articles are governed by the applicable Creative Commons License

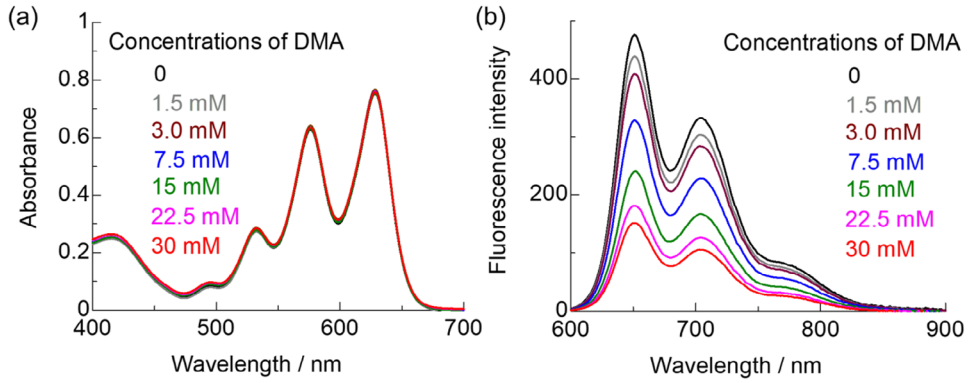

FIGURE 6 | (a) UV–vis–NIR absorption and (b) fluorescence spectra of **5** in dichloromethane (3.0×10^{-5} M) with varying concentrations of DMA (0, 1.5 3.0 7.5, 15, 22.5 and 30 mM). Fluorescence spectra were recorded with an excitation wavelength of 500 nm.

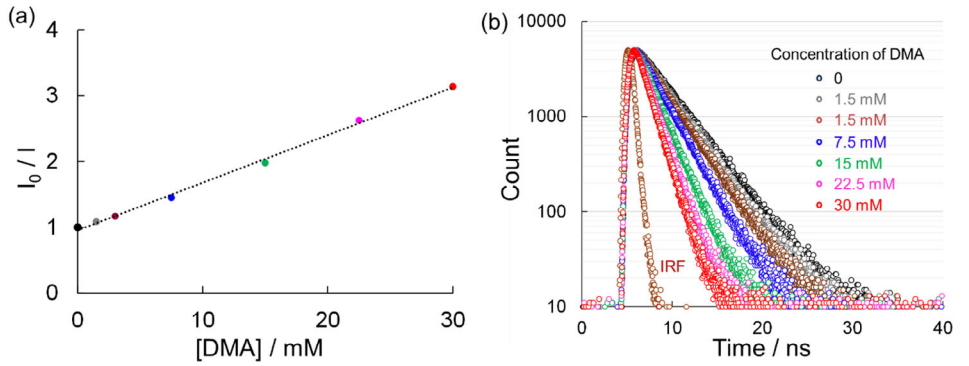

FIGURE 7 | (a) Stern–Volmer plot for steady-state fluorescence quenching of **5** by DMA. (b) Changes in the fluorescence decays of the **5** as a function of DMA concentration. Time-resolved fluorescence measurements were performed at an excitation wavelength of 470 nm. The fluorescence decay curves were analyzed by reconvolution fitting using the measured instrument response function (IRF).

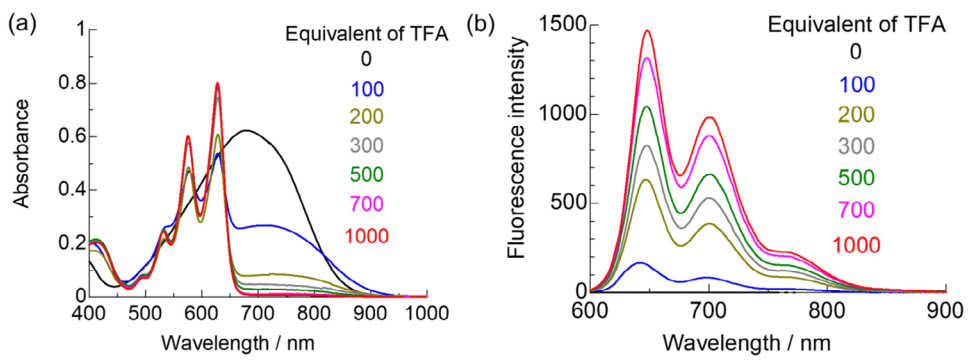

FIGURE 8 | (a) UV–vis–NIR absorption and (b) fluorescence spectra of **8** in dichloromethane (3.0×10^{-5} M) with varying equivalents of TFA (0, 100, 200, 300, 500, 1000 equiv.).

in dichloromethane upon addition of TFA are shown in Figure 8a. As the equivalents of added TFA increased, the absorption at 680 nm, assigned to **8**, decreased, and four new peaks appeared at 626, 575, 531, and 494 nm. The TDDFT calculations indicate that the S_0–S_1 transitions of the monoprotonated form **9'** (λ_{max} = 881 nm) and the diprotonated form **9** (λ_{max} = 603 nm) are both dominated by HOMO–LUMO transitions, exhibiting significant bathochromic and hypsochromic shifts, respectively, relative to **8** (λ_{max} = 704 nm) (Figure S9). On this basis, the newly emerged absorption bands at 626, 575, 531, and 494 nm upon addition of TFA are assigned to the $S_{0,0}$–$S_{1,0}$, $S_{0,0}$–$S_{1,1}$, $S_{0,0}$–$S_{1,2}$, and $S_{0,0}$–$S_{1,3}$ transitions of the diprotonated form **9**, respectively. The absence of an isosbestic point in the absorption spectra upon addition of TFA indicates the involvement of an intermediate species, namely, the monoprotonated form **9'** [76, 77]. Additionally, no absorption attributable to **9'** was observed in the longer-wavelength region, suggesting that **9'** is rapidly converted to **9** upon formation. Furthermore, fluorescence at 648 nm emerged

15213765, 2026, 34, Downloaded from https://chemistry-europe.onlinelibrary.wiley.com/doi/10.1002/chem.71179 by Okayama University, Wiley Online Library on [19/11/2026]. See the Terms and Conditions (https://onlinelibrary.wiley.com/terms-and-conditions) on Wiley Online Library for rules of use; OA articles are governed by the applicable Creative Commons License

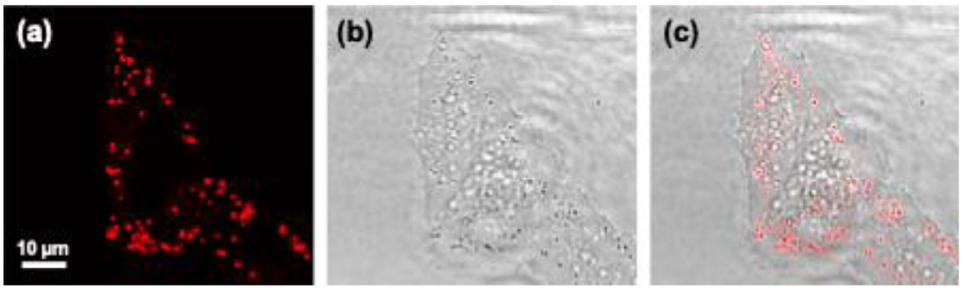

FIGURE 9 | (a) Confocal fluorescence image of live HeLa cells stained with **5** (500 nM). Acquisition conditions: $\lambda_{ex} = 561$ nm and $\lambda_{em} = 600–700$ nm. (b) Bright field. (c) Merged image. Scale bar: 10 μm.

upon addition of TFA, with the intensity increasing as the amount of TFA was increased (Figure 8b). The excitation spectrum of **8** upon addition of excess TFA showed good agreement with the absorption spectrum of the diprotonated form **9** (Figure S10a). The fluorescence decay was well fitted with a single-exponential function (Figure S10b). These results indicate that the observed emission predominantly originates from the diprotonated form **9**, with negligible contribution from **9'**. This fluorescence behavior is attributed to protonation of the dimethylamino groups, which converts the electron-donating groups into electron-withdrawing groups, thereby suppressing the intramolecular PeT process.

In our previous study, the 1,5-diboron complex showed no fluorescence, even in the phenyl-substituted derivative (Figure S3) [60]. Its λ_{max} value (694 nm) is shifted to longer wavelengths compared with the corresponding 1,4-diboron complex **5** (628 nm). According to the energy gap law, the 1,5-diboron complex is more prone to nonradiative deactivation than the 1,4-diboron complex, which likely contributes to its nonfluorescent behavior [78, 79]. Additionally, DFT calculations suggest that the electronic structure of the 1,5-diboron complex differs from that of the 1,4-diboron complex, with the HOMO energy level being lower (Figure S11). These calculation results are considered to reflect differences in the electronic structures of the dye backbones. Taking into account the experimentally observed nonfluorescent behavior, in the 1,5-diboron complex, not only the enhancement of nonradiative deactivation associated with the red shift of the absorption wavelength but also a nonradiative deactivation process related to intramolecular PeT may be involved [80, 81].

6 | Cell Imaging

The potential of 1,4-diboron complex **5** for cellular imaging was subsequently investigated. Due to its poor water solubility, we first measured the fluorescence spectrum in an aqueous medium containing a nonionic surfactant Cremophor EL (CrEL) [82, 83]. In this medium, **5** exhibited fluorescence with a maximum at 637 nm and vibronic peaks at 693 nm and approximately 760 nm (Figure S12), indicating that fluorescence was retained under these aqueous conditions.

Following this, the staining behavior of **5** was evaluated in live HeLa cells. Cells were incubated with **5** (500 nM) in DMEM containing 10% fetal bovine serum (FBS) in a 5% CO_2 incubator and then observed by confocal fluorescence microscopy without washing (Figure 9). Under these conditions, punctate intracellular fluorescence was readily observed even after 10 min incubation, demonstrating efficient cellular uptake of **5**. Co-staining with LipiDye II showed substantial signal overlap, with a correlation coefficient of $R = 0.89$, indicating that, due to its hydrophobicity, **5** preferentially localizes to lipid droplets in living cells (Figure S13). In contrast, fluorescence images of fixed cells showed broadly distributed fluorescence, suggesting that fixation affects the subcellular distribution of **5** (Figure S14).

We also assessed the cytotoxicity of **5** using an MTT assay. After 24 h of incubation, a modest concentration-dependent decrease in cell viability was observed at concentrations ranging from 0.25 to 2 μM (Figure S15). At the staining concentration used for imaging (500 nM), the reduction in viability remained limited, supporting the applicability of **5** for fluorescence imaging under the present conditions.

7 | Conclusions

In summary, N^O-type 1,4-diboron complexes derived from 1,4-bis(arylamino)anthraquinones exhibit near-infrared fluorescence, in clear contrast to the previously reported non-emissive 1,5-diboron analogues. The fluorescence quantum yields decrease with increasing electron-donating ability of the substituents, which is attributed to enhanced nonradiative decay via intramolecular PeT. This interpretation is supported by fluorescence quenching experiments using DMA and theoretical calculations, which reveal a correlation between electronic structure and nonradiative decay processes. In addition, protonation studies demonstrate that suppression of intramolecular PeT effectively restores fluorescence, further confirming its key role in the deactivation pathway. Comparison with 1,5-diboron systems suggests that their non-emissive nature originates from more efficient intramolecular PeT combined with energy gap law effects associated with red-shifted absorption. These findings provide deeper insight into the structure–property relationship governing emissive behavior in diboron complexes of anthraquinone and offer useful guidelines for the molecular design of near-infrared emissive materials.

8 | Experimental Section

8.1 | General Information

NMR spectra were recorded using JEOL ECX400P and ECA600 spectrometers. Infrared (IR) spectra were determined on a

15213765, 2026, 34, Downloaded from https://chemistry-europe.onlinelibrary.wiley.com/doi/10.1002/chem.71179 by Okayama University, Wiley Online Library on [19/11/2026]. See the Terms and Conditions (https://onlinelibrary.wiley.com/terms-and-conditions) on Wiley Online Library for rules of use; OA articles are governed by the applicable Creative Commons License

Simazu IR–Affinity spectrometer. UV–vis–NIR absorption spectra were recorded using a Hitachi U4100 and a Shimadzu UV-3600i Plus spectrophotometer. Mass spectra were recorded on a JEOL JMS–700 spectrometer. Elemental analyses were performed on a Yanaco MT–6 CHN corder. Melting points were measured on a Yanagimoto MP–S2 micro–melting–point apparatus. Analytical thin-layer chromatography (TLC) was performed on pre-coated plates (Merck, silica gel 60 F254). Silica gel (Wakogel C–200) was used for column chromatography.

8.2 | X-Ray Crystallography

Single-crystal X-ray diffraction measurements were carried out with a Rigaku Mercury 375R/M CCD (XtaLAB-mini) diffractometer with graphite-monochromated Mo Kα radiation (λ = 0.71075 Å). The crystal structure was solved using direct method with SHELXT-2018/2 [84] and refined by full matrix least-squaresmethods with anisotropic thermal parameters for nonhydrogen atoms on F^2 using SHELXL-2018/3 [85]. Hydrogen atoms were placed at calculated positions and refined applying riding models. The Cambridge Crystallographic Data Center (CCDC) number for **5** is 2457602.

Crystallographic details for **5**: $C_{26}H_{16}B_2F_4N_2O_2$, M = 486.03 g mol^{-1}; T = 293(2) K; monoclinic, space group $P2_1/n$; a = 13.964(3), b = 9.580(2), c = 17.066(5) Å, α = 90, β = 101.196(10), γ = 90°; V = 2239.6(9) Å^3; Z = 4; 2.974< θ < 27.594; ρ_{calcd} = 1.441 g cm^{-3}; μ = 0.113 mm^{-1}; R_{int} = 0.0611; R_1 = 0.0595, wR_2 = 0.1595 for 5003 reflections with $I > 2\sigma$(I) and 325 parameters; S = 1.027; CCDC 2457602.

8.3 | Cell Experiments

8.3.1 | Cell Culture

HeLa (RCB0007) cells were obtained from RIKEN Cell Bank. The cells were cultured in Dulbecco's Modified Eagle's Medium (DMEM; low glucose, with *L*-glutamine and sodium pyruvate; Wako, 041–29775) supplemented with 10% fetal bovine serum (FBS; Biosera, 554–02155) and 1% Antibiotic-Antimycotic (AA; Wako, 161–23181) at 37 °C in a humidified 5% CO_2 incubator. For imaging experiments, cells (2×10^4 cells/dish) were seeded in glass-bottom dishes or 96-well glass plates two days before observation.

8.3.2 | Fluorescence Microscopy

Live-cell imaging: Cells were incubated with **5** (500 nM) in DMEM(+) containing 1% DMSO for 10 min at 37 °C in a CO_2 incubator and then subjected to confocal fluorescence imaging without washing. Fluorescence images were acquired with a FLUOVIEW FV3000 (Evident) confocal laser-scanning microscope equipped with 405, 488, 561, 640, and 730 nm lasers, GaAsP PMT and GaAs PMT detectors, and a TruFocus Red Z-drift compensator. For co-staining experiments, cells were stained with **5** (500 nM) and 1 µM LipiDye II (Funakoshi). The acquisition parameters are given in the corresponding figure captions.

Fixed-cell imaging: Cells were washed with PBS, fixed with 4% paraformaldehyde (PFA) in PBS at room temperature for 30 min, and washed three times with culture medium. The fixed cells were then stained with **5** (10 µM) in PBS containing Cremophor EL (CrEL) and imaged using a KEYENCE BZ-X800 microscope.

8.4 | MTT Assay

HeLa cells were seeded into 96-well plates (2×10^3 cells/well) and cultured in DMEM(+) at 37 °C for 2 days. The medium was then replaced with DMEM containing **5** at concentrations of 0, 0.25, 0.5, 1.0, and 2.0 µM (0.5% DMSO). After a 24 h incubation, MTT reagent was added to each well (final concentration: 0.5 mg/mL), and the plates were incubated for an additional 2 h. The wells were then washed with PBS to remove excess reagent, and the resulting formazan crystals were dissolved in DMSO (200 µL/well) with shaking for 10 min at room temperature. Absorbance at 530 nm was measured using a SpectraMax i3 plate reader (Molecular Devices). Results are expressed as percentages relative to the dye-free control.

8.5 | Synthesis of 1,4-bis(Anilino)Anthraquinone (1) [61]

1,4-dihydroxyanthraquinone (1.00 g, 4.16 mmol), aniline (4.26 g, 45.7 mmol), boric acid (100 mg, 1.62 mmol), zinc powder (60 mg, 0.92 mmol) and conc. HCl (0.40 mL, 12.9 mmol) were mixed and heated at 100°C for 16 h. The reaction mixture was quenched with water, extracted with DCM, dried over Na_2SO_4 and evaporated under reduced pressure. Column chromatography of the residue on silica gel (DCM: hexane = 1:1) gave **1** (550 mg, Y = 34%) as a purple solid. ^{1}H NMR (400 MHz, $CDCl_3$) δ 7.17 (t, J = 7.3 Hz, 2H), 7.28 (d, J = 7.3 Hz, 4H), 7.39 (dd, J = 7.3, 7.3 Hz, 4H), 7.51 (s, 2H), 7.77 (dd, J = 5.7, 3.7 Hz, 2H), 8.39 (dd, J = 5.7, 3.7 Hz, 2H), 12.2 (s, 2H); ^{13}C NMR (100 Hz, $CDCl_3$) δ 111.61, 123.82, 123.96, 124.65, 124.77, 124.87, 124.92, 126.29, 126.38, 129.47, 129.56, 132.72, 134.34, 139.53, 143.78, 183.52; IR (KBr) 1597, 1578, 1558, 1504, 1366, 1261, 1169, 1072, 1026, 729, 689 cm^{-1}.

8.6 | Synthesis of 1,4-bis(4-trifluoromethylanilino)Anthraquinone (2)

1,4-dihydroxyanthraquinone (502 mg, 2.09 mmol), 4-trifluoromethylaniline (3.72 g, 23.1 mmol), boric acid (51 mg, 0.83 mmol), zinc powder (30 mg, 0.46 mmol) and conc. HCl (0.40 mL, 12.9 mmol) were mixed and heated at 100°C for 5 h. The reaction mixture was quenched with water, extracted with DCM, dried over Na_2SO_4 and evaporated under reduced pressure. Column chromatography of the residue on silica gel (DCM: hexane = 1:1) gave **4** (180 mg, Y = 16%) as a purple solid. mp: 284–285°C; ^{1}H NMR (400 MHz, $CDCl_3$) δ 7.36 (d, J = 8.0 Hz, 4H), 7.63 (d, J = 8.0 Hz, 4H), 7.63 (s, 2H), 7.79 (dd, J = 6.0, 3.3 Hz, 2H), 8.35 (dd, J = 6.0, 3.3 Hz, 2H), 12.1 (s, 2H); ^{13}C NMR (100 MHz, $CDCl_3$) δ 113.57, 121.99, 122.10, 124.13 (q, J = 270.8 Hz), 124.74, 125.74 (q, J = 32.4 Hz), 126.53, 126.62, 126.81, 133.40, 134.02, 142.15, 143.14, 184.55; ^{19}F NMR (376 MHz, $CDCl_3$) δ -61.91 (s, 6F); IR (KBr) 1612, 1578, 1512, 1323, 1265, 1161, 1111, 1072, 829, 729 cm^{-1};

15213765, 2026, 34, Downloaded from https://chemistry-europe.onlinelibrary.wiley.com/doi/10.1002/chem.71179 by Okayama University, Wiley Online Library on [19/11/2026]. See the Terms and Conditions (https://onlinelibrary.wiley.com/terms-and-conditions) on Wiley Online Library for rules of use; OA articles are governed by the applicable Creative Commons License

HRMS (FAB) *m/z* calcd for $C_{28}H_{17}F_6N_2O_2$ $[M + H]^+$ 527.1189, found 527.1151.

8.7 | Synthesis of 1,4-bis(4-methoxyanilino)Anthraquinone (3) [62]

1,4-dihydroxyanthraquinone (1.02 g, 4.25 mmol), 4-methoxyaniline (5.65 g, 45.9 mmol), boric acid (101 mg, 1.63 mmol), zinc powder (62 mg, 0.95 mmol) and conc. HCl (0.40 mL, 12.9 mmol) were mixed and heated at 100°C for 5 h. The reaction mixture was quenched with water, extracted with DCM, dried over Na_2SO_4 and evaporated under reduced pressure. Column chromatography of the residue on silica gel (DCM) gave **3** (887 mg, Y = 46%) as a purple solid. ^{1}H NMR (400 MHz, $CDCl_3$) δ 3.83 (s, 6H), 6.93 (d, J = 8.9 Hz, 4H), 7.19 (d, J = 8.9 Hz, 4H), 7.31 (s, 2H), 7.76 (dd, J = 6.0, 3.2 Hz, 2H), 8.40 (dd, J = 6.0, 3.2 Hz, 2H), 12.2 (s, 2H); ^{13}C NMR (100 Hz, $CDCl_3$) δ 55.45, 55.58, 110.59, 114.68, 114.45, 124.88, 126.28, 126.39, 132.16, 132.45, 134.45, 144.93, 157.25, 182.95; IR (KBr) 1597, 1578, 1558, 1512, 1362, 1296, 1250, 1165, 1072, 1038, 818, 725 cm^{-1}.

8.8 | Synthesis of 1,4-bis(4-dimethylaminoanilino)Anthraquinone (4) [63]

1,4-dihydroxyanthraquinone (2.00 g, 8.32 mmol), *N*,*N*-dimethyl-*p*-phenylenediamine (8.52 g, 62.6 mmol), boric acid (200 mg, 3.24 mmol), zinc powder (120 mg, 1.84 mmol) and conc. HCl (0.80 mL, 25.8 mmol) were mixed and heated at 100°C for 10 h. The reaction mixture was quenched with water, extracted with DCM, dried over Na_2SO_4 and evaporated under reduced pressure. Column chromatography of the residue on silica gel (DCM: EtOAc = 10:1) gave **2** (1.67 g, Y = 42%) as a blue solid. ^{1}H NMR (400 MHz, $CDCl_3$) δ 2.97 (s, 12H), 6.75 (d, J = 8.8 Hz, 4H), 7.14 (d, J = 8.8 Hz, 4H), 7.31 (s, 2H), 7.74 (dd, J = 5.8, 3.8 Hz, 2H), 8.41 (dd, J = 5.8, 3.8 Hz, 2H), 12.3 (s, 2H); ^{13}C NMR (100 Hz, $CDCl_3$) δ 40.76, 40.85, 110.07, 113.22, 125.21, 126.20, 126.31, 128.36, 132.16, 134.57, 145.54, 148.54, 182.31; IR (KBr) 1613, 1585, 1547, 1520, 1504, 1366, 1261, 1165, 1134, 826, 729 cm^{-1}.

8.9 | Synthesis of 5

Boron trifluoride diethyl ether complex (2 mL, 16 mmol) were added to a solution of **1** (390 mg, 1.00 mmol) in *o*-xylene (300 mL). After refluxing for 1 day, the reaction mixture was quenched with water, extracted with DCM, dried over Na_2SO_4 and evaporated under reduced pressure. Column chromatography of the residue on silica gel (DCM) gave **5** (507 mg, Y = 80%) as a blue solid.

mp: 285–286°C; ^{1}H NMR (400 MHz, $CDCl_3$) δ 7.08 (s, 2H), 7.36 (d, J = 6.9 Hz, 4H), 7.44–7.52 (m, 6H), 7.95 (dd, J = 7.9, 3.2 Hz, 2H), 8.72 (dd, J = 7.9, 3.2 Hz, 2H); ^{13}C NMR (100 Hz, $CDCl_3$) δ 125.17, 126.81, 129.13, 129.71, 130.46, 132.50, 133.17, 138.41, 152.68, 154.18, 159.40; ^{11}B NMR (128 MHz, $CDCl_3$) δ 0.35 (t, J = 13.5 Hz, 2B); ^{19}F NMR (376 MHz, $CDCl_3$) δ -127.8 (q, J = 13.5 Hz, 4F); IR (KBr) 1582, 1524, 1485, 1308, 1227, 1184, 1141, 1111, 1045, 1003, 698 cm^{-1}; EIMS (70 eV) *m/z* (rel intensity) 448 (13), 486 (M^+, 100); Anal. Found: C, 64.04; H, 3.55; N, 5.84%. Calcd for $C_{26}H_{16}B_2F_4N_2O_2$: C, 64.25; H, 3.32; N, 5.76%.

8.10 | Synthesis of 6

Boron trifluoride diethyl ether complex (2 mL, 16 mmol) were added to a solution of **2** (526 mg, 1.00 mmol) in *o*-xylene (300 mL). After refluxing for 1 day, the reaction mixture was quenched with water, extracted with DCM, dried over Na_2SO_4 and evaporated under reduced pressure. Column chromatography of the residue on silica gel (DCM) gave **6** (423 mg, Y = 68%) as a blue solid.

mp: 298–299°C; ^{1}H NMR (400 MHz, $CDCl_3$) δ 7.08 (s, 2H), 7.51 (d, J = 8.2 Hz, 4H), 7.79 (d, J = 8.2 Hz, 4H), 7.99 (dd, J = 6.4, 3.3 Hz, 2H), 8.74 (dd, J = 6.4, 3.3 Hz, 2H); ^{13}C NMR (150 MHz, $CDCl_3$) δ 123.46 (q, J = 270.1 Hz), 127.00, 127.03, 127.28, 127.56, 130.61, 131.51 (q, J = 33.1 Hz), 132.52, 133.91, 141.50, 149.40, 153.84, 161.01; ^{11}B NMR (128 MHz, $CDCl_3$) δ 0.33 (t, J = 14.7 Hz, 2B); ^{19}F NMR (376 MHz, $CDCl_3$) δ -126.83 (q, J = 14.7 Hz, 4F), -62.66 (s, 6F); IR (KBr) 1582, 1523, 1485, 1327, 1169, 1130, 1111, 1069, 1049 cm^{-1}; EIMS (70 eV) *m/z* (rel intensity) 622 (M^+, 18), 584 (100), 526 (51), 439 (30); Anal. Found: C, 54.18; H, 2.30; N, 4.63%. Calcd for $C_{28}H_{14}B_2F_{10}N_2O_2$: C, 54.06; H, 2.27; N, 4.50%.

8.11 | Synthesis of 7

Boron trifluoride diethyl ether complex (2 mL, 16 mmol) were added to a solution of **3** (450 mg, 1.00 mmol) in *o*-xylene (300 mL). After refluxing for 5 h, the reaction mixture was quenched with water, extracted with DCM, dried over Na_2SO_4 and evaporated under reduced pressure. Column chromatography of the residue on silica gel (DCM) gave **7** (448 mg, Y = 82%) as a blue solid.

Melting point (mp) >300°C; ^{1}H NMR (400 MHz, $CDCl_3$) δ 3.86 (s, 6H), 7.01 (d, J = 9.0 Hz, 4H), 7.15 (s, 2H), 7.29 (d, J = 9.0 Hz, 4H), 7.93 (dd, J = 6.2, 3.5 Hz, 2H), 8.71 (dd, J = 6.2, 3.5 Hz, 2H); ^{13}C NMR (100 Hz, $CDCl_3$) δ 55.57, 55.71, 114.84, 114.96, 126.68, 126.75, 127.81, 127.93, 130.37, 131.22, 132.38, 132.94, 154.24, 158.80, 160.06; ^{11}B NMR (128 MHz, $CDCl_3$) δ 0.33 (t, J = 12.3 Hz, 2B); ^{19}F NMR (376 MHz, $CDCl_3$) δ -128.7 (q, J = 12.3 Hz, 4F); IR (KBr) 1605, 1582, 1508, 1477, 1300, 1254, 1180, 1138, 1107, 1053, 1026, 995, 841 cm^{-1}; EIMS (70 eV) *m/z* (rel intensity) 368 (16), 508 (28), 546 (M^+, 100); Anal. Found: C, 61.24; H, 3.73; N, 5.18%. Calcd for $C_{28}H_{20}B_2F_4N_4O_2$: C, 61.58; H, 3.69; N, 5.13%.

8.12 | Synthesis of 8

Boron trifluoride diethyl ether complex (2 mL, 16 mmol) were added to a solution of **4** (477 mg, 1.00 mmol) in *o*-xylene (300 mL). After refluxing for 5 h, the reaction mixture was quenched with water, extracted with DCM, dried over Na_2SO_4 and evaporated under reduced pressure. Column chromatography of the residue on silica gel (DCM) gave **8** (475 mg, Y = 83%) as a blue solid.

Melting point (mp) >300°C; ^{1}H NMR (400 MHz, $CDCl_3$) δ 3.03 (s, 12H), 6.76 (d, J = 8.8 Hz, 4H), 7.22 (s, 2H), 7.25 (d, J = 8.8 Hz, 4H), 7.88 (dd, J = 6.3, 3.3 Hz, 2H), 8.70 (dd, J = 6.3, 3.3 Hz, 2H); ^{13}C NMR (100 Hz, $CDCl_3$) δ 40.34, 40.43, 112.30, 126.30, 126.36, 127.45, 127.56,

15213765, 2026, 34, Downloaded from https://chemistry-europe.onlinelibrary.wiley.com/doi/10.1002/chem.71179 by Okayama University, Wiley Online Library on [19/11/2026]. See the Terms and Conditions (https://onlinelibrary.wiley.com/terms-and-conditions) on Wiley Online Library for rules of use; OA articles are governed by the applicable Creative Commons License

127.70, 130.11, 131.52, 132.19, 134.57, 150.61, 153.52, 157.08; ^{11}B NMR (128 MHz, $CDCl_3$) δ 0.31 (t, J = 13.5 Hz, 2B); ^{19}F NMR (376 MHz, $CDCl_3$) δ -131.2 (q, J = 13.5 Hz, 4F); IR (KBr) 1601, 1520, 1481, 1366, 1300, 1188, 1107, 1045 cm^{-1}; EIMS (70 eV) m/z (rel intensity) 572 (M^+, 61), 534 (100); Anal. Found: C, 62.66; H, 4.23; N, 9.76%. Calcd for $C_{30}H_{26}B_2F_4N_4O_2$: C, 62.97; H, 4.58; N, 9.79%.

Acknowledgments

This work was partially supported by JSPS KAKENHI Grant Numbers JP20K18602 and JP23K04873.

Conflicts of Interest

The authors declare no conflicts of interest.

Data Availability Statement

The data that supports the findings of this study are available in the supplementary material of this article

References

1. L. J. Patalag, H. F. Koeller, and D. B. Werz, "Bioapplications of Small Molecule Aza-BODIPY: From Rational Structural Design to In Vivo Investigations," *Organic Materials* 2024, 6, 78–89.

2. Y. Kubota, *Progress in the Science of Functional Dyes*, ed. Y. Ooyama and S. Yagi (Springer, 2021), 119–220.

3. Z. Shi, X. Han, W. Hu, et al., "Bioapplications of Small Molecule Aza-BODIPY: From Rational Structural Design to In Vivo Investigations," *Chemical Society Reviews* 49 (2020): 7533–7567.

4. H. Lu, J. Mack, Y. Yang, and Z. Shen, "Structural Modification Strategies for the Rational Design of Red/NIR Region BODIPYs," *Chemical Society Reviews* 43 (2014): 4778–4823.

5. D. Frath, J. Massue, G. Ulrich, and R. Ziessel, "Luminescent Materials: Locking π-Conjugated and Heterocyclic Ligands With Boron(III)," *Angewandte Chemie International Edition* 53 (2014): 2290–2310.

6. N. Boens, V. Leen, and W. Dehaen, "Fluorescent Indicators Based on BODIPY," *Chemical Society Reviews* 41 (2012): 1130–1172.

7. J. Wang, W. Li, L. Jiao, and E. Hao, "Ring-Fused BODlPY Derived Heavy-Atom-Free Triplet Photosensitizers," *Chemical Communications* 61 (2025): 4465–4482.

8. J. G. Becerra-González, E. Peña-Cabrera, and J. Belmonte-Vázquez, "From Blue to Red. Reaching the Full Visible Spectrum With a Single Fluorophore: BODIPY," *Tetrahedron* 168 (2024): 134334.

9. Z. Mao, J. H. Kim, J. Lee, H. Xiong, F. Zhang, and J. S. Kim, "Engineering of BODIPY-Based Theranostics for Cancer Therapy," *Coordination Chemistry Reviews* 476 (2023): 214908.

10. V. K. Shukla, G. Chakraborty, A. K. Ray, and S. Nagaiyan, "Red and NIR Emitting Ring-Fused BODIPY/Aza-BODIPY Dyes," *Dyes and Pigments* 215 (2023): 111245.

11. G. Ulrich, R. Ziessel, and A. Harriman, "The Chemistry of Fluorescent Bodipy Dyes: Versatility Unsurpassed," *Angewandte Chemie International Edition* 47 (2008): 1184–1201.

12. A. Loudet and K. Burgess, "BODIPY Dyes and Their Derivatives: Syntheses and Spectroscopic Properties," *Chemical Reviews* 107 (2007): 4891–4932.

13. S. Sultan, L. Crovetto, and R. Rios, "Recent Advances in the Development of Enantiopure BODIPYs and Some Related Enantiomeric Compounds," *Chemical Communications* 61 (2025): 1989–2010.

14. L. M. Stevens, N. T. Almada, H. S. Kim, and Z. A. Page, "Visible-Light-Fueled Polymerizations for 3D Printing," *Accounts of Chemical Research* 58 (2025): 250–260.

15. D. Pinjari, Y. Patil, and R. Misra, "Near-Infrared Absorbing Aza-BODIPY Dyes for Optoelectronic Applications," *Chemistry – An Asian Journal* 19 (2024): e202400167.

16. C. Liu, L. Yin, and Y. Li, "Organoboron-Embedded Functional Materials: Recent Developments in Photovoltaic and Luminescence Properties," *Journal of Materials Chemistry C* 12 (2024): 11723–11751.

17. R. Segovia-Pérez, M. Ibarra-Rodríguez, B. M. Muñoz-Flores, and V. M. Jiménez-Pérez, "Near-Infrared Fluorescent BODIPY Dyes: Green Synthesis, Photophysical Properties, and Their Applications in Biomedical Molecular Imaging," *Dyes and Pigments* 239 (2025): 112740.

18. H. Ahmad, S. Muhammad, M. Mazhar, et al., "Unveiling Cellular Mysteries: Advances in BODIPY Dyes for Subcellular Imaging," *Coordination Chemistry Reviews* 526 (2025): 216383.

19. Y. Dai, J. Sun, X. Zhang, et al., "Supramolecular Assembly Boosting the Phototherapy Performances of BODIPYs," *Coordination Chemistry Reviews* 517 (2024): 216054.

20. C. S. Mahanta, V. Ravichandiran, and S. P. Swain, "Recent Developments in the Design of New Water-Soluble Boron Dipyrromethenes and Their Applications: an Updated Review," *ACS Applied Bio Materials* 6 (2023): 2995–3018.

21. A. N. Bismillah and I. Aprahamian, "Fundamental Studies to Emerging Applications of Pyrrole-BF_2 (BOPHY) Fluorophores," *Chemical Society Reviews* 50 (2021): 5631–5649.

22. J. Wang, X. Fang, X. Guo, et al., "Sterically Protected and Conformation-Restricted BOBHY Dyes With Bright Near-Infrared Fluorescence: N_2 O-Type Expanded BOPHY Dyes Derived from Boronic Acids," *Organic Letters* 23 (2021): 4796–4801.

23. T. Zhang, J. Yan, Y. Hu, et al., "A Simple Central Seven-Membered BOPYIN: Synthesis, Structural, Spectroscopic Properties, and Cellular Imaging Application," *Chemistry – A European Journal* 25 (2019): 9266–9271.

24. R. R. Maar, R. Zhang, D. G. Stephens, Z. Ding, and J. B. Gilroy, "Near-Infrared Photoluminescence and Electrochemiluminescence From a Remarkably Simple Boron Difluoride Formazanate Dye," *Angewandte Chemie International Edition* 58 (2019): 1052–1056.

25. Y. Kubota, M. Tsukamoto, K. Ohnishi, J. Jin, K. Funabiki, and M. Matsui, "Synthesis and Fluorescence Properties of Novel Squarylium–boron Complexes," *Organic Chemistry Frontiers* 4 (2017): 1522–1527.

26. L. J. Patalag, P. G. Jones, and D. B. Werz, "BOIMPYs: Rapid Access to a Family of Red-Emissive Fluorophores and NIR Dyes," *Angewandte Chemie International Edition* 55 (2016): 13340–13344.

27. R. Yoshii, A. Hirose, K. Tanaka, and Y. Chujo, "Functionalization of Boron Diiminates With Unique Optical Properties: Multicolor Tuning of Crystallization-Induced Emission and Introduction into the Main Chain of Conjugated Polymers," *Journal of the American Chemical Society* 136 (2014): 18131–18139.

28. D. Li, H. Zhang, and Y. Wang, "Four-Coordinate Organoboron Compounds for Organic Light-Emitting Diodes (OLEDs)," *Chemical Society Reviews* 42 (2013): 8416.

29. M. Shahid, J. Wertz, I. Degano, M. Aceto, M. I. Khan, and A. Quye, "Analytical Methods for Determination of Anthraquinone Dyes in Historical Textiles: A Review," *Analytica Chimica Acta* 1083 (2019): 58–87.

30. E. S. B. Ferreira, A. N. Hulme, H. McNab, and A. Quye, "The Natural Constituents of Historical Textile Dyes," *Chemical Society Reviews* 33 (2004): 329.

31. S. Benkhaya, S. M' rabet, and A. El Harfi, "A Review on Classifications, Recent Synthesis and Applications of Textile Dyes," *Inorganic Chemistry Communications* 115 (2020): 107891.

15213765, 2026, 34, Downloaded from https://chemistry-europe.onlinelibrary.wiley.com/doi/10.1002/chem.71179 by Okayama University, Wiley Online Library on [19/11/2026]. See the Terms and Conditions (https://onlinelibrary.wiley.com/terms-and-conditions) on Wiley Online Library for rules of use; OA articles are governed by the applicable Creative Commons License

32. L. Dufossé, "Anthraquinones, the Dr Jekyll and Mr Hyde of the Food Pigment family," *Food Research International* 65 (2014): 132–136.

33. W. Tian, C. Wang, D. Li, and H. Hou, "Novel Anthraquinone Compounds as Anticancer Agents and Their Potential Mechanism," *Future Medicinal Chemistry* 12 (2020): 627–644.

34. C. Zhao, W. Lu, A. Aziz, M. Asif, C. Dong, and S. Shuang, "A Neoteric Smartphone-Assisted Colorimetric and Fluorometric Dual-Mode Probe Based on Anthraquinone Derived Schiff Base for Wide-Range pH and Cu^{2+}/S^{2-} Determination in Bioimaging," *Biosensors and Bioelectronics* 271 (2025): 117085.

35. T. P. Martyanov, A. A. Kudrevatykh, E. N. Ushakov, et al., "Selective Colorimetric Sensor for Cyanide Anion Based on 1-Hydroxyanthraquinone," *Tetrahedron* 93 (2021): 132312.

36. P. O. Gupta and N. Sekar, "NLOphoric Anthraquinone Dyes – A Review," *ChemistrySelect* 9 (2024): e202400736.

37. E. I. L. Jull, M. Wahle, P. J. M. Wyatt, et al., "Efficiency Improvements in a Dichroic Dye-Doped Liquid Crystal Fresnel Lens," *Optics Express* 27 (2019): 26799.

38. Z. Chen and T. M. Swager, "Synthesis and Characterization of Fluorescent Acenequinones as Dyes for Guest−Host Liquid Crystal Displays," *Organic Letters* 9 (2007): 997–1000.

39. Q. Miao, Z. Cao, Y. Liu, et al., "Hydrogen Radical-Driven Anthraquinone-Promoted H_2O_2 Photosynthesis," *Chemical Engineering Journal* 508 (2025): 160957.

40. J. M. Campos-Martin, G. Blanco-Brieva, and J. L. G. Fierro, "Hydrogen Peroxide Synthesis: An Outlook Beyond the Anthraquinone Process," *Angewandte Chemie International Edition* 45 (2006): 6962–6984.

41. A. N. Dias, *Journal of Photochemistry and Photobiology A: Chemistry* 53 (1990): 141–167.

42. Y. Li, T. Tan, S. Wang, Y. Xiao, and X. Li, "Highly Solvatochromic Fluorescence of Anthraquinone Dyes Based on Triphenylamines," *Dyes and Pigments* 144 (2017): 262–270.

43. T. Kuwabara, J. Orii, Y. Segawa, and K. Itami, "Curved Oligophenylenes as Donors in Shape-Persistent Donor–Acceptor Macrocycles With Solvatofluorochromic Properties," *Angewandte Chemie International Edition* 54 (2015): 9646–9649.

44. L. Zhang, S. Zhou, S. Min, et al., "Water-Soluble Near-Infrared Fluorescent Probes Enhanced by Ionic co-Assembly of a Four-Armed Amphiphile with SDBS: Toward Application in Cell Imaging," *Dyes and Pigments* 181 (2020): 108541.

45. J. Zhang, R. Chen, Z. Zhu, C. Adachi, X. Zhang, and C.-S. Lee, "Highly Stable Near-Infrared Fluorescent Organic Nanoparticles With a Large Stokes Shift for Noninvasive Long-Term Cellular Imaging," *ACS Applied Materials & Interfaces* 7 (2015): 26266–26274.

46. B. Huang, W.-C. Chen, Z. Li, et al., "Manipulation of Molecular Aggregation States to Realize Polymorphism, AIE, MCL, and TADF in a Single Molecule," *Angewandte Chemie International Edition* 57 (2018): 12473–12477.

47. B. Huang, Z. Li, H. Yang, et al., "Bicolour Electroluminescence of 2-(Carbazol-9-yl)anthraquinone Based on a Solution Process," *Journal of Materials Chemistry C* 5 (2017): 12031–12034.

48. T. Wang, Z. Tang, D. Xu, et al., "Waterborne Polyacrylates With Thermally Activated Delayed Fluorescence and Two-State Phosphorescence," *Materials Chemistry Frontiers* 2 (2018): 559–565.

49. Q. Zhang, H. Kuwabara, W. J. Potscavage, et al., "Anthraquinone-Based Intramolecular Charge-Transfer Compounds: Computational Molecular Design, Thermally Activated Delayed Fluorescence, and Highly Efficient Red Electroluminescence," *Journal of the American Chemical Society* 136 (2014): 18070–18081.

50. G. Feng, W. Wu, S. Xu, and B. Liu, "Far Red/Near-Infrared AIE Dots for Image-Guided Photodynamic Cancer Cell Ablation," *ACS Applied Materials & Interfaces* 8 (2016): 21193–21200.

51. J. Miguel-Ávila, M. Tomás-Gamasa, and J. L. Mascareñas, "Intracellular Ruthenium-Promoted (2+2+2) Cycloadditions," *Angewandte Chemie International Edition* 59 (2020): 17628–17633.

52. L. Hou, X. Kong, Y. Wang, et al., "An Anthraquinone-Based Highly Selective Colorimetric and Fluorometric Sensor for Sequential Detection of Cu^{2+} and S^{2-} With Intracellular Application," *Journal of Materials Chemistry B* 5 (2017): 8957–8966.

53. Y. Ji, Z. Li, N. Zhou, et al., "Simple Aggregation–induced Delayed Fluorescence Materials Based on Anthraquinone Derivatives for Highly Efficient Solution–processed Red OLEDs," *Journal of Luminescence* 187 (2017): 414–420.

54. P. N. Preston, T. Winwick, and J. O. Morley, "Selective Dealkylation of Methoxyanthraquinones via Difluoro[1-Hydroxymethoxyanthraquinonato-O 1,O 9]Boron Chelates: Synthesis of Hydroxymethoxyanthraquinones," *Journal of the Chemical Society, Perkin Transactions 1* 1983 (1983): 1439.

55. P. N. Preston, T. Winwick, and J. O. Morley, "Selective Demethylation of Di- and Tri-Methoxyanthraquinones via Aryloxydifluoroboron Chelates. Synthesis of 4-Hydroxy-1,5-Dimethoxyanthraquinone and 1,4-Dihydroxy-5-Methoxyanthraquinone," *Journal of the Chemical Society, Chemical Communications* 1983 (1983): 89.

56. Y. Zhou, Y. Zheng, O. Zeika, H. Hartmann, and K. Leo, "On the Doping of Zinc Phthalocyanine with 2,2′-Difluoro-1,3,2-Dioxaborines Derived from Halo-Substituted Quinizarines," *Materials Chemistry and Physics* 112 (2008): 577–579.

57. M. V. Gorelik, N. N. Shapet'ko, L. V. Arinich, A. I. Tsurkan, and M. L. Kukushkina, "Structure of the borate complexes of α-amino- and α-hydroxy-9,10-anthraquinones and their reaction with amines," *Zhurnal Organicheskoi Khimii* 22 (1986): 611–621.

58. K. Ono, J. Hashizume, H. Yamaguchi, M. Tomura, J. Nishida, and Y. Yamashita, "Synthesis, Crystal Structure, and Electron-Accepting Property of the BF_2 Complex of a Dihydroxydione With a Perfluorotetracene Skeleton," *Organic Letters* 11 (2009): 4326–4329.

59. K. Ono, H. Yamaguchi, K. Taga, K. Saito, J. Nishida, and Y. Yamashita, "Synthesis and Properties of BF_2 Complexes to Dihydroxydiones of Tetracene and Perylene: Novel Electron Acceptors Showing n-Type Semiconducting Behavior," *Organic Letters* 11 (2009): 149–152.

60. Y. Kubota, A. Ogasawara, S. Mizuno, T. Inuzuka, and K. Funabiki, "Synthesis of Anthraquinone Mono- and Diboron Complexes With Near-Infrared Panchromatic Absorption," *Chemistry – A European Journal* 31 (2025): e01915.

61. M. Matsui, A. Sedyohutomo, M. Satoh, et al., "Solubility and Decomposition Temperature of 1,4-Bis(arylamino)Anthraquinone Dyes," *Dyes and Pigments* 40 (1998): 21–26.

62. A. H. Cook and W. Waddington, "99. Experiments in the Coeroxene and Coeramidine Series," *Journal of the Chemical Society (Resumed)* (1945): 402.

63. M. Ichikawa and M. Okazaki, "Quaternary Ammonium Salts Derived From 1, 4-Disubstituted Anthraquinone," *Journal of the Society of Chemical Industry, Japan* 67 (1964): 138–142.

64. P. Sykes, *A Guidebook to Mechanism in Organic Chemistry*, 5th edn (Longman, 1981).

65. M. J. Frisch, G. W. Trucks, H. B. Schlegel, et al., "Gaussian 09, Revision A. 02," Gaussian, Inc. Wallingford, CT, 2009.

66. R. E. Stratmann, G. E. Scuseria, and M. J. Frisch, "An Efficient Implementation of Time-Dependent Density-Functional Theory for the Calculation of Excitation Energies of Large Molecules," *Journal of Chemical Physics* 109 (1998): 8218–8224.

67. M. E. Casida, C. Jamorski, K. C. Casida, and D. R. Salahub, "Molecular Excitation Energies to High-Lying Bound States from Time-Dependent Density-Functional Response Theory: Characterization and Correction of the Time-Dependent Local Density Approximation

15213765, 2026, 34, Downloaded from https://chemistry-europe.onlinelibrary.wiley.com/doi/10.1002/chem.71179 by Okayama University, Wiley Online Library on [19/11/2026]. See the Terms and Conditions (https://onlinelibrary.wiley.com/terms-and-conditions) on Wiley Online Library for rules of use; OA articles are governed by the applicable Creative Commons License

Ionization Threshold," *Journal of Chemical Physics* 108 (1998): 4439–4449.

68. R. Bauernschmitt and R. Ahlrichs, "Treatment of Electronic Excitations Within the Adiabatic Approximation of Time Dependent Density Functional Theory," *Chemical Physics Letters* 256 (1996): 454–464.

69. V. V. Pavlishchuk and A. W. Addison, "Conversion Constants for Redox Potentials Measured versus Different Reference Electrodes in Acetonitrile Solutions at 25°C," *Inorganica Chimica Acta* 298 (2000): 97–102.

70. T. Lin and B.-X. Peng, "Synthesis and Spectral Characteristics of Some Highly Soluble Squarylium Cyanine Dyes," *Dyes and Pigments* 35 (1997): 331–338.

71. A. Hori, A. Matsumoto, J. Ikenouchi, and G. Konishi, "D–π–A Fluorophores With Strong Solvatochromism for Single-Molecule Ratiometric Thermometers," *Journal of the American Chemical Society* 147 (2025): 9953–9961.

72. Y. Kubota, Y. Sakuma, K. Funabiki, and M. Matsui, "Solvatochromic Fluorescence Properties of Pyrazine–Boron Complex Bearing a β-Iminoenolate Ligand," *Journal of Physical Chemistry A* 118 (2014): 8717–8729.

73. M. H. Gehlen, "The Centenary of the Stern-Volmer Equation of Fluorescence Quenching: from the Single Line Plot to the SV Quenching Map," *Journal of Photochemistry and Photobiology C: Photochemistry Reviews* 42 (2020): 100338.

74. P. Verma and H. Pal, "Tuning of Electron Transfer Reactions in Pluronic–surfactant Supramolecular Assemblies," *Physical Chemistry Chemical Physics* 17 (2015): 15400–15411.

75. T. Ghosh, S. Chatterjee, and E. Prasad, "Photoinduced Electron Transfer From Various Aniline Derivatives to Graphene Quantum Dots," *Journal of Physical Chemistry A* 119 (2015): 11783–11790.

76. Y. Deng, T. Albert, C. Van Stappen, et al., "Unveiling an Ultrareduced State of Heme in Myoglobin," *Journal of the American Chemical Society* 147 (2025): 29983–29993.

77. B.-Y. Wang, T. Žujović, D. A. Turner, C. M. Hadad, and J. D. Badjić, "Design, Preparation, and Study of Catalytic Gated Baskets," *Journal of Organic Chemistry* 77 (2012): 2675–2688.

78. S. R. L. Fernando, U. S. M. Maharoof, K. D. Deshayes, T. H. Kinstle, and M. Y. Ogawa, "A Negative Activation Energy for Luminescence Decay: Specific Solvation Effects on the Emission Properties of Bis(2,2′-Bipyridine)(3,5-Dicarboxy-2,2′-Bipyridine)Ruthenium(II) Chloride," *Journal of the American Chemical Society* 118 (1996): 5783–5790.

79. J. V. Caspar, B. P. Sullivan, E. M. Kober, and T. J. Meyer, "Application of the Energy Gap Law to the Decay of Charge Transfer Excited States, Solvent Effects," *Chemical Physics Letters* 91 (1982): 91–95.

80. H. Sunahara, Y. Urano, H. Kojima, and T. Nagano, "Design and Synthesis of a Library of BODIPY-Based Environmental Polarity Sensors Utilizing Photoinduced Electron-Transfer-Controlled Fluorescence ON/OFF Switching," *Journal of the American Chemical Society* 129 (2007): 5597–5604.

81. A. P. de Silva, H. Q. N. Gunaratne, T. Gunnlaugsson, et al., "Signaling Recognition Events With Fluorescent Sensors and Switches," *Chemical Reviews* 97 (1997): 1515–1566.

82. A. Janiga, E. Glodkowska-Mrowka, T. Stoklosa, and D. T. Gryko, "Synthesis and Optical Properties of Tetraaryl-1,4-Dihydropyrrolo[3,2- b]Pyrroles," *Asian Journal of Organic Chemistry* 2 (2013): 411–415.

83. A. Gorman, J. Killoran, C. O'Shea, T. Kenna, W. M. Gallagher, and D. F. O'Shea, "In Vitro Demonstration of the Heavy-Atom Effect for Photodynamic Therapy," *Journal of the American Chemical Society* 126 (2004): 10619–10631.

84. G. M. Sheldrick, "SHELXT – Integrated Space-Group and Crystal-Structure Determination," *Acta Crystallographica Section A Foundations and Advances* 71 (2015): 3–8.

85. G. M. Sheldrick, "Crystal Structure Refinement With SHELXL," *Acta Crystallographica Section C Structural Chemistry* 71 (2015): 3–8.

Supporting Information

Additional supporting information can be found online in the Supporting Information section.

Supporting file 1: chem71179-sup-0001-SuppMat.pdf

Supporting file 2: chem71179-sup-0002-cif.zip

15213765, 2026, 34, Downloaded from https://chemistry-europe.onlinelibrary.wiley.com/doi/10.1002/chem.71179 by Okayama University, Wiley Online Library on [19/11/2026]. See the Terms and Conditions (https://onlinelibrary.wiley.com/terms-and-conditions) on Wiley Online Library for rules of use; OA articles are governed by the applicable Creative Commons License